

# ArchKalMag14k: A Kalman-filter based global geomagnetic model for the Holocene

Maximilian Arthus Schanner<sup>1</sup>, Monika Korte<sup>1</sup>, and Matthias Holschneider<sup>2</sup>

<sup>1</sup>GFZ German Research Center for Geosciences

<sup>2</sup>University of Potsdam

November 22, 2022

## Abstract

We propose a global geomagnetic field model for the last fourteen thousand years, based on thermoremanent records. We call the model ArchKalMag14k. ArchKalMag14k is constructed by modifying recently proposed algorithms, based on space-time correlations. Due to the amount of data and complexity of the model, the full Bayesian posterior is numerically intractable. To tackle this, we sequentialize the inversion by implementing a Kalman-filter with a fixed time step. Every step consists of a prediction, based on a degree dependent temporal covariance, and a correction via Gaussian process regression. Dating errors are treated via a noisy input formulation. Cross-correlations are re-introduced by a smoothing algorithm and model parameters are inferred from the data. Due to the specific statistical nature of the proposed algorithms, the model comes with space and time dependent uncertainty estimates. The new model ArchKalMag14k shows less variation in the large scale degrees than comparable models. Local predictions represent the underlying data and agree with comparable models, if the location is sampled well. Uncertainties are bigger for earlier times and in regions of sparse data coverage. We also use ArchKalMag14k to analyze the appearance and evolution of the South Atlantic anomaly together with reverse flux patches at the core mantle boundary, considering the model uncertainties. While we find good agreement with earlier models for recent times, our model suggests a different evolution of intensity minima prior to 1650 CE. In general, our results suggest that prior to 6000 BCE the database is not strong enough to support global models.

1                   **ArchKalMag14k: A Kalman-filter based global**  
2                   **geomagnetic model for the Holocene**

3                   **M. Schanner<sup>1</sup>, M. Korte<sup>1</sup>, M. Holschneider<sup>2</sup>**

4                   <sup>1</sup>German Research Centre for Geosciences GFZ, Section 2.3, Potsdam, Germany

5                   <sup>2</sup>Applied Mathematics, University of Potsdam, Potsdam, Germany

6                   **Key Points:**

- 7                   • We propose a new global geomagnetic field model for the Holocene based on ther-  
8                   moremanent records.
- 9                   • Existing algorithms based on space-time correlation are modified by sequential-  
10                  ization via a Kalman-filter and smoothing.
- 11                  • The results suggest that prior to 6000 BCE the database is not strong enough to  
12                  support global models.

---

Corresponding author: M. Schanner, [arthus@gfz-potsdam.de](mailto:arthus@gfz-potsdam.de)

**Abstract**

We propose a global geomagnetic field model for the last fourteen thousand years, based on thermoremanent records. We call the model ArchKalMag14k. ArchKalMag14k is constructed by modifying recently proposed algorithms, based on space-time correlations. Due to the amount of data and complexity of the model, the full Bayesian posterior is numerically intractable. To tackle this, we sequentialize the inversion by implementing a Kalman-filter with a fixed time step. Every step consists of a prediction, based on a degree dependent temporal covariance, and a correction via Gaussian process regression. Dating errors are treated via a noisy input formulation. Cross-correlations are re-introduced by a smoothing algorithm and model parameters are inferred from the data. Due to the specific statistical nature of the proposed algorithms, the model comes with space and time dependent uncertainty estimates.

The new model ArchKalMag14k shows less variation in the large scale degrees than comparable models. Local predictions represent the underlying data and agree with comparable models, if the location is sampled well. Uncertainties are bigger for earlier times and in regions of sparse data coverage. We also use ArchKalMag14k to analyze the appearance and evolution of the South Atlantic anomaly together with reverse flux patches at the core mantle boundary, considering the model uncertainties. While we find good agreement with earlier models for recent times, our model suggests a different evolution of intensity minima prior to 1650 CE. In general, our results suggest that prior to 6000 BCE the database is not strong enough to support global models.

**Plain Language Summary**

We use data of archaeological and volcanic origin from the last fourteen thousand years to construct a global geomagnetic field model. We call the model ArchKalMag14k. The database is uneven in space, with significantly more records in the Northern hemisphere and multiple clusters. Further, the number of available records decreases in time with a distinct drop 6000 BCE. Previous studies introduced a modeling method that was adapted to this inhomogeneities, but could not be applied to the whole database for computational reasons. To tackle this, we modify the method and implement an approach which handles only a number of records at a time. Relations between the individual steps are re-introduced later in the algorithm. Uncertainties in the data and in their ages contribute to estimating reasonable model uncertainties. The model parameters are inferred from the data.

ArchKalMag14k shows less variation on a global scale than comparable models. On a local scale, predictions represent the underlying data and agree with comparable models, if the location is covered well by data. Uncertainties are bigger for times and regions of sparse data coverage. The results suggest that prior to 6000 BCE the database is not strong enough to support global models.

**1 Introduction**

Global field reconstructions of the past are a key tool for understanding the dynamics of the Earth's magnetic field and the underlying processes in the Earth's core (e.g. C. Constable & Korte, 2015). This includes studying the evolution of field features, such as dipole decay, the South Atlantic Anomaly (SAA) and flux patches (Hartmann & Pacca, 2009; Jackson & Finlay, 2015). In the past, several techniques for constructing global field models have been developed and employed. Truncated spherical harmonics (SH) in the spatial domain combined with spline interpolation in time are widely used (Jackson et al., 2000; Korte et al., 2009; Senftleben, 2019). In the eighties, C. G. Constable and Parker (1988) first proposed using Gaussian processes to model the field dynamics, but until recently, the technique had not been applied to global field modeling. Only in the last years,

62 statistical methods implementing this approach have been suggested (Hellio & Gillet,  
63 2018; Nilsson & Suttie, 2021).

64 While early models (Jackson et al., 2000; C. G. Constable et al., 2000; Korte & Con-  
65 stable, 2003) do not provide uncertainty estimates, more recent field models use ensem-  
66 ble techniques to quantify (modeling related) errors (Korte et al., 2009; Licht et al., 2013;  
67 Pavón-Carrasco et al., 2014; Hellio & Gillet, 2018; Senftleben, 2019). In contrast, Nilsson  
68 and Suttie (2021) (and earlier Hellio et al. (2014) for local field models) used a Bayesian  
69 formulation of the proposed Gaussian process (GP) approach, to estimate uncertainties  
70 based on the posterior distribution.

71 Holschneider et al. (2016) extended the GP approach to the spatial domain, to also  
72 reflect uncertainties resulting from the data distribution, and in two recent studies this  
73 method was adapted to paleomagnetic records (Mauerberger et al., 2020; M. Schanner  
74 et al., 2021). The major challenge with the modeling strategies proposed there is related  
75 to the inversion of large scale matrices, and the methods were found computationally un-  
76 feasible for the number of records available for the Holocene. In the area of modeling the  
77 recent field, this challenge was overcome by applying sequentialization by means of a Kalman-  
78 filter (Kalman, 1960) to the inversion problem (Baerenzung et al., 2020; Ropp et al., 2020).  
79 This way, models from a way higher number of satellite observations have been constructed,  
80 while retaining the strategies proposed by Holschneider et al. (2016). In this study we  
81 apply sequentialization to the earlier developed strategy (M. Schanner et al., 2021, in  
82 the following referred to as SMK21) and propose a new global geomagnetic field model  
83 for the Holocene.

84 Usually, global geomagnetic field models are inferred from two classes of data: Data  
85 from materials with thermoremanent magnetisation, such as volcanic rocks, bricks or burnt  
86 clay fragments from archeologic sites, and data from marine or lacustrine sediments with  
87 embedded magnetic particles. In this paper we focus on the former class and loosely re-  
88 fer to it as archeomagnetic data. The extension to sediments poses several additional chal-  
89 lenges, some of which are addressed and discussed by Nilsson and Suttie (2021). The a priori  
90 model that results from the sequentialization of SMK21 is similar to the one proposed  
91 by Nilsson and Suttie (2021). Besides a focus on a different and smaller dataset, the main  
92 difference lies in the inversion procedure: While Nilsson and Suttie (2021) employ a prob-  
93 abilistic Markov Chain Monte-Carlo (MCMC) based strategy, we rely on a determinis-  
94 tic inversion based on Kalman-filtering.

95 The rest of this article is structured as follows: In Section 2 we discuss prior as-  
96 sumptions, showcase the modeling method and introduce the dataset. Section 3 contains  
97 a brief validation section, using synthetic data, but mainly focuses on the description of  
98 features of the new model, which are discussed in section 4. We conclude in Section 5  
99 by reconsidering possible extensions and shortcomings of the method, as well as an out-  
100 look to future work.

## 101 2 Method and Data

### 102 2.1 Gaussian process based modeling

103 In the eighties C. G. Constable and Parker (1988) proposed using GPs to model  
104 the Earth’s magnetic field (EMF). The technique was later applied by Gillet et al. (2013)  
105 and extended by Holschneider et al. (2016). A GP is a stochastic process that is uniquely  
106 characterized by a mean function  $\bar{\mathbf{B}}$  and a covariance function  $K_{\mathbf{B}}$

$$107 \mathbf{B} \sim \mathcal{GP}(\bar{\mathbf{B}}, K_{\mathbf{B}}) . \quad (1)$$

108 Gaussian process based modeling is a Bayesian approach, where a GP is used as a prior  
109 and an update is given by some normal likelihood, relating observations to the magnetic  
field. The posterior is then a GP as well, so that the model is also uniquely character-

110 ized by a mean function and a covariance function (Rasmussen & Williams, 2006). The  
 111 main difficulty in applying this technique to paleomagnetic records lies in constructing  
 112 the normal likelihood, as archeomagnetic observations are non-linearly related to the mag-  
 113 netic field.

## 114 2.2 Data model

115 To apply GP based modeling, one has to construct a normal likelihood, relating  
 116 observations to the magnetic field. In paleomagnetism, the observations are the field di-  
 117 rections (declination  $D$  and inclination  $I$ ) and intensity  $F$ . At locations  $\mathbf{x}$  and times  $t$ ,  
 118 the data model can then be formulated as

$$o(\mathbf{x}) = \mathbf{H}(\mathbf{B}(\mathbf{x}, t)) + \mathbf{E} , \quad (2)$$

119 where the observation functional  $\mathbf{H} = (D, I, F)$  contains the usual expressions for dec-  
 120 lination, inclination and intensity and  $\mathbf{E}$  are the observation errors. This data model is  
 121 not Gaussian, as  $\mathbf{H}$  is non-linear. We linearize the observation functional, to construct  
 122 a normal proxy for the data model (2):

$$D \approx \tilde{D} + \frac{1}{\tilde{F}_H^2} \begin{bmatrix} -\tilde{B}_E \\ \tilde{B}_N \\ 0 \end{bmatrix}^\top \mathbf{B} , \quad (3)$$

$$I \approx \tilde{I} + \frac{1}{\tilde{F}_H} \left( \begin{bmatrix} 0 \\ 0 \\ 1 \end{bmatrix} - \frac{\tilde{B}_Z \tilde{\mathbf{B}}}{\tilde{F} \tilde{F}} \right)^\top \mathbf{B} , \quad (4)$$

$$F \approx \frac{\tilde{\mathbf{B}}^\top}{\tilde{F}} \mathbf{B} . \quad (5)$$

123  $\tilde{D}, \tilde{I}, \tilde{F}$  and  $\tilde{\mathbf{B}}$  indicate the point of expansion (POE) and we summarize the linearized  
 124 expressions as  $\mathbf{H}_{\text{lin}}$ . The observation errors  $\mathbf{E}$  are also non-Gaussian, as the directional  
 125 errors are given by a Fisher-von Mises distribution. We approximate this two dimensional  
 126 distribution with 95% confidence cone ( $\alpha_{95}$ ) by two centered normal distributions with  
 127 standard deviations (Piper, 1989; Suttie & Nilsson, 2019)

$$\sigma_I = \frac{57.3^\circ}{140} \alpha_{95} \quad \text{and} \quad \sigma_D = \frac{1}{\cos \theta_I} \sigma_I . \quad (6)$$

128 We label these approximate errors  $\mathbf{E}_{\text{prox}}$ . Next, we consider dating uncertainties as sug-  
 129 gested in SMK21. The precise times  $t$  at which the archeomagnetic specimen received  
 130 their magnetization are unknown. Instead, a corrupted date  $t_o = t + e_t$  is reported,  
 131 and we consider  $e_t$  to be a centered normal error. This error in the inputs is handled by  
 132 another linearization, as proposed by McHutchon and Rasmussen (2011, the noisy in-  
 133 put Gaussian process (NIGP)). As the errors are centered, the a priori mean is not af-  
 134 fected by this procedure. However, via linearization the dating uncertainties are trans-  
 135 lated into observation uncertainties, and the covariance gets an additional term

$$\Sigma_{tt'} \circ \partial_t \partial_{t'} K_{\mathbf{B}}(\mathbf{x}, \mathbf{x}')|_{t_o} . \quad (7)$$

136 Here  $\Sigma_{tt'}$  is the dating error covariance matrix and  $\circ$  is the Hadamard product, i.e. el-  
 137 ement wise multiplication along the  $t$  direction. To this end,  $K_{\mathbf{B}}(\mathbf{x}, \mathbf{x}')$  is considered as  
 138 a matrix consisting of  $3 \times 3$  blocks. The effect of the NIGP model is thus the inclusion  
 139 of dating errors as contributions to the data covariance, similar to measurement errors.  
 140 The translation is realized by weighing the dating uncertainties by the second order time  
 141 derivative of the kernel. This is related, but not equal, to the idea of using the secular  
 142 variation to estimate the contribution of dating uncertainties (see e.g. Korte et al., 2005).  
 143 Due to the GP structure of the proposed model, the covariance structure for the secu-  
 144 lar variation is available a priori. Finally, a residual term is added to cover any effects

145 that are not modeled, like crustal field or ellipticity of the Earth. This way, the data model  
146 reads

$$o(\mathbf{x}) \approx \mathbf{H}_{\text{lin.}} \left( \mathbf{B}(\mathbf{x}, t_o) - e_t^\top \partial_t \mathbf{B}(\mathbf{x}, t)|_{t_o} + \rho \mathbf{P} \right) + \mathbf{E}_{\text{prox.}} . \quad (8)$$

### 147 2.3 A priori process

148 We consider the common SH expansion of the geomagnetic potential  $\Phi$ , which is  
149 valid outside of the Earth’s conducting core, assuming an insulating mantle:

$$\Phi(\mathbf{x}) = R \sum_{\ell} \left( \frac{R}{|\mathbf{x}|} \right)^{\ell+1} \sum_{-\ell \leq m \leq \ell} g_{\ell}^m(t) Y_{\ell}^m(\hat{\mathbf{x}}) . \quad (9)$$

150  $\hat{\mathbf{x}}$  is the unit vector  $\mathbf{x}/|\mathbf{x}|$  and  $Y_{\ell}^m$  refers to the real valued and Schmidt semi-normalized  
151 SH of degree  $\ell$  and order  $m$  with related Gauss coefficient  $g_{\ell}^m$ . From this, the Earth’s  
152 magnetic field is given as the gradient

$$\mathbf{B} = -\nabla \Phi , \quad (10)$$

153 and mean and covariance function of the EMF can be derived from assumptions about  
154 correlations of the Gauss coefficients. A priori we assume all Gauss coefficients except  
155 for the axial dipole to be of zero mean. The axial dipole is assumed constant, with value  
156  $\gamma_1^0$ . We assume all coefficients to be uncorrelated at a reference radius  $R = 2800$  km  
157 within the Earth’s core. This is the “virtual” source region where the field is uncorre-  
158 lated, with no direct physical meaning. The magnetic field given by this assumption is  
159 only a valid representation of the actual field above the core-mantle boundary (CMB).  
160 Inside of the core it can be seen as an artificial connection of the physical field at the CMB  
161 to the virtual sources inside of the core. We assume two different a priori variances, one  
162 for the dipole coefficients  $\alpha_{\text{DP}}$  and one for all higher degrees  $\alpha_{\text{ND}}$ . For each coefficient  
163 we assume a temporal correlation in the form of an AR(2)-process, as proposed by Gillet  
164 et al. (2013) and employed also by others (Hellio & Gillet, 2018; Baerenzung et al., 2020;  
165 Ropp et al., 2020; Nilsson & Suttie, 2021). This way, the temporal correlation of each  
166 coefficient is given by

$$\rho_{\ell}(t - t') = \left( 1 + \frac{|t - t'|}{\tau_{\ell}} \right) \exp \left( -\frac{|t - t'|}{\tau_{\ell}} \right) . \quad (11)$$

167 Similar to Baerenzung et al. (2020), we assume one correlation time  $\tau_{\text{DP}}$  for the dipole  
168 and a relation for all higher degrees  $\ell \geq 2$

$$\tau_{\ell} = \frac{\tau_{\text{ND}}}{\ell} . \quad (12)$$

169 The posterior may be smoother or more detailed than these scales, depending on the data.

### 170 2.4 Sequentialization

171 In previous studies (Mauerberger et al., 2020; M. Schanner et al., 2021) we aimed  
172 at performing standard GP regression in the introduced setting. However, as determin-  
173 ing the hyperparameters of the model requires this regression to be performed many times,  
174 this proved to be computationally unfeasible. To overcome this, we perform a sequen-  
175 tialized inversion, in form of a Kalman filter (Kalman, 1960; Baerenzung et al., 2020).  
176 Starting at an initial time, the Kalman filter consists of a series of steps, each consist-  
177 ing of a prediction based on the current model and a correction, which updates the model  
178 if data is available. In contrast to the previous study SMK21, this requires us to de-  
179 fine a cutoff degree  $\ell_{\text{max}}$ , so that the model can be characterized by a finite vector of co-  
180 efficients and their derivatives  $\mathbf{z} = (g_{\ell}^m, \dot{g}_{\ell}^m)$ . The prediction equations from step  $i$  to  
181  $i + 1$  are given by

$$\mathbb{E}[z_{i+1|i}] = \mathbf{F}_i \mathbb{E}[z_i] \quad (13)$$

$$\text{Cov}[z_{i+1|i}, z_{i+1|i}] = \mathbf{F}_i \text{Cov}[z_i, z_i] \mathbf{F}_i^\top + \tilde{\Sigma} , \quad (14)$$

where

$$F_i(\ell, \Delta t = t_{i+1} - t_i) = \begin{pmatrix} 1 + |\Delta t|/\tau_\ell & \Delta t \\ -\Delta t/\tau_\ell^2 & 1 - |\Delta t|/\tau_\ell \end{pmatrix} \exp\left(-\frac{|\Delta t|}{\tau_\ell}\right)$$

182 is the forward operator of the AR(2)-process and  $\tilde{\Sigma} = \Sigma - \mathbf{F}\Sigma\mathbf{F}^\top$  with the a priori  
 183 correlations  $\Sigma$ . The correction step consists of a Bayesian GP inversion, as described in  
 184 detail in SMK21. The linearization is performed around the current model, beginning  
 185 with the prior. We run the Kalman filter “backwards”, i.e. from modern times to the past,  
 186 as the data distribution is sparser towards earlier years. We expect the bigger amount  
 187 of data in the beginning of the filtering to constrain the model and improve the POE for  
 188 earlier times. We choose a cutoff degree of  $\ell_{\max} = 20$  and a step size of  $\Delta t = 10$  years.  
 189 Both choices are believed to allow for a way higher resolution than present in the data,  
 190 so that every dynamic present in the data can be captured by the model. After running  
 191 the Kalman-filter we run a smoothing algorithm, following the formulation of Rauch et  
 192 al. (1965) (see also Baerenzung et al. (2020)). This way, cross correlations that are not  
 193 present in the Kalman-filter are re-introduced to the posterior.

194 We store a set of coefficients every 50 years, so that the output of a sequentialized  
 195 inversion consists of 281 sets of 440 main field coefficients, 440 secular variation coeffi-  
 196 cients and the respective covariances.

## 197 2.5 Hyperparameters

198 The a priori model depends on several parameters, that have to be inferred before  
 199 the actual inversion can be performed. One approach (e.g. Helliö & Gillet, 2018; Nils-  
 200 son & Suttie, 2021) is to infer these parameters from outside knowledge, for example from  
 201 models based on observatory and satellite data. We followed this approach in selecting  
 202 the reference radius  $R$ , which effectively controls the slope of the a priori spectrum, by  
 203 comparison to the IGRF models. For the other parameters we suggest a more self-consistent  
 204 strategy and estimate them based on a maximum likelihood procedure. This strategy  
 205 did not work for the reference radius, most likely because the sparse data in earlier years  
 206 do not constrain it well enough.

207 Consider the forward log-marginal likelihood

$$\mathcal{L}_{\text{fwd.}} = \sum_{i=1}^n \left[ -\ln |\Sigma_{o,i}| - \frac{1}{2} (o_i - \mathbf{H}_{\text{lin.}} \mathbf{B}(\mathbf{z}_i))^\top \Sigma_{o,i}^{-1} (o_i - \mathbf{H}_{\text{lin.}} \mathbf{B}(\mathbf{z}_i)) \right] \quad (15)$$

with observations  $o$  and observation covariance  $\Sigma_o$ . The forward likelihood depends on  
 the hyperparameters and is considered a measure for how good a choice of hyperparam-  
 eters describes the data. We maximize this expression using LIPO-TR (King, 2009, 2017)  
 and use the maximum estimator for the parameters in the inference. The search region  
 is specified by lower and upper bounds for the hyperparameters, these are as follows:

$$\begin{aligned} -100 \mu\text{T} \leq \gamma_1^0 \leq -10 \mu\text{T} & & 1 \mu\text{T} \leq \alpha_\bullet \leq 1000 \mu\text{T} \\ 10 \text{ yrs.} \leq \tau_\bullet \leq 2000 \text{ yrs.} & & 0.01 \mu\text{T} \leq \rho \leq 5 \mu\text{T} \end{aligned}$$

208 where  $\bullet$  stands for DP and ND.

## 209 2.6 Dataset

210 The dataset is a slight variation of all records from the archaeological and volcanic  
 211 database from GEOMAGIA v3.4 (Brown et al., 2015) with ages between 12000 BCE and  
 212 2000 CE. Some of the records from Mexico contain wrong age and dating uncertainty  
 213 estimates (Mahgoub, pers. comm.), so they have been altered or removed, if no better  
 214 estimate was available. To identify records that deviate from the rest, we use a Naive  
 215 Bayes classifier. This procedure is integrated into the Kalman-filter as follows:

216 When a step  $i+1$  contains new data, we evaluate the probability of every record  
 217 to either come from a normal distribution with standard deviation of the size of the re-  
 218 ported error or from a flat distribution of larger variance ( $(100^\circ)^2$  for declination,  $(50^\circ)^2$   
 219 for inclination and  $(100\mu\text{T})^2$  for intensities). Records that are more likely to stem from  
 220 the flat distribution are considered outliers. In comparison to the standard approach of  
 221 rejecting all data that deviates by a specific amount from the model, this procedure is  
 222 more flexible and allows larger deviations, especially if the current model reports high  
 223 uncertainties. By this procedure 276 records are identified and removed from the dataset.  
 224 The final dataset contains 18735 records from 11637 locations. It consists of 5611 de-  
 225 clinations, 7028 inclinations and 6096 intensities.

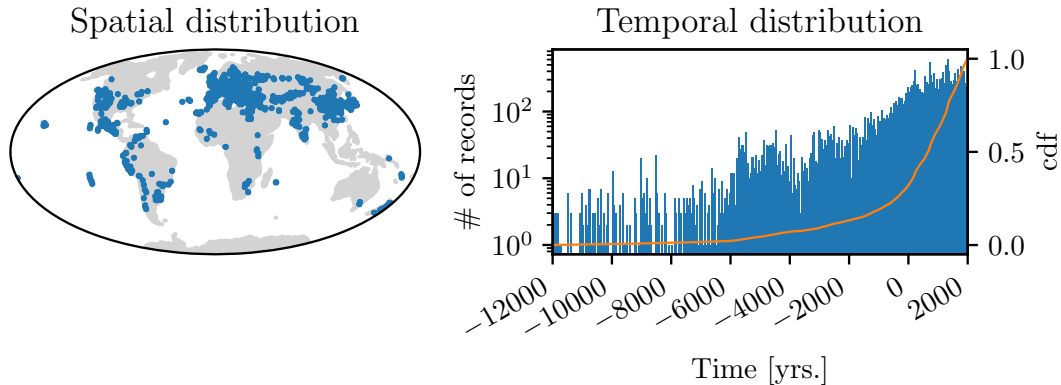


**Figure 1.** Spatial and temporal distribution of the data. Every declination, inclination and intensity is counted as one record and represented by one dot. Note the logarithmic scale (left) on the histogram. To emphasize the inhomogeneity in the temporal distribution, the normalized cumulative sum of the data is shown in orange (right scale).

## 226 3 Results

### 227 3.1 Validation

228 In order to validate the proposed modeling method, we performed a test inversion  
 229 on synthetic data. We therefore set up a model with fixed hyperparameters and sam-  
 230 pled coefficients from the prior distribution, which serve as reference. From these coef-  
 231 ficients we generated data at the same input locations and times as the ones in the dataset  
 232 described in section 2.6. The data was then corrupted by artificial noise from a Gamma  
 233 distribution for the intensity and a von Mises-Fisher distribution for the directions and  
 234 by normal noise in the ages. The error levels reported in the database were used. Ta-  
 235 ble 1 shows the fixed hyperparameters and the inferred ones. Apart from one parame-  
 236 ter they agree reasonably well. The deviance in the non-dipole correlation time is likely  
 237 due to the data distribution. We believe that the inferred a priori correlation time is suf-  
 238 ficient to resolve the variations that are present in the data. No additional contributions  
 239 (white noise) were added to the synthetic dataset and the algorithm chooses the lowest  
 240 possible value for the residual scaling accordingly.

241 Figure 2 shows generated and inferred axial dipole and quadrupole. Again, a promis-  
 242 ing agreement is observed, although some variation in the dipole, prominently between  
 243 10000 and 8000 BCE, is not resolved in the inferred model. This already hints at the data  
 244 not containing enough information to recover global features during early times. Fur-  
 245 ther figures from the validation process, showing the other dipole and some higher or-  
 246 der coefficients, are available with the supplementary material.

**Table 1.** Hyperparameters that have been used to generate synthetic data for the validation (“fixed”) and the ones inferred using the proposed method.<sup>2</sup>

Model	$\gamma_1^0$ [ $\mu\text{T}$ ]	$\alpha_{\text{DP}}$ [ $\mu\text{T}$ ]	$\tau_{\text{DP}}$ [yrs.]	$\alpha_{\text{ND}}$ [ $\mu\text{T}$ ]	$\tau_{\text{ND}}$ [yrs.]	$\rho$ [ $\mu\text{T}$ ]
Fixed	-412.3	13.8	250	39.4	393	-
Inferred	-408.55	9.87	302.48	30.70	724.76	0.01

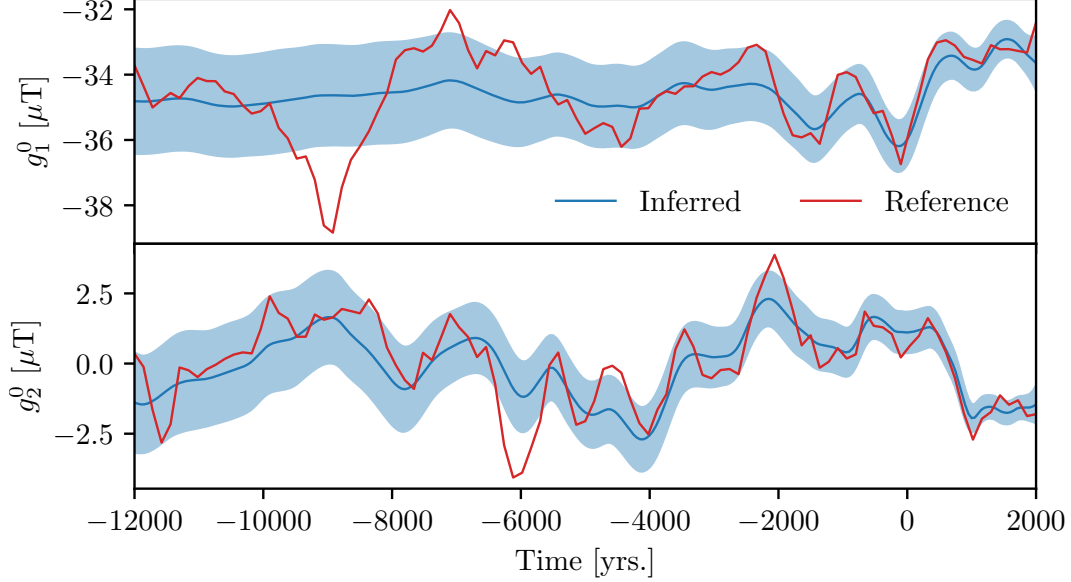


**Figure 2.** Axial dipole (top) and quadrupole (bottom) of the synthetic model, together with the corresponding inferred ones from the proposed inversion. The inferred (blue) and reference curves (red) agree within the one-sigma region shown in light blue. Some variations, most prominently in the axial dipole between 10000 and 8000 BCE, can not be resolved.

247

### 3.2 ArchKalMag14k

248

249

250

251

252

253

254

In the following we propose and describe a new global geomagnetic field model, based on archeomagnetic records. It covers the last 14000 years and we call it ArchKalMag-14k, as it is based on methods similar to the KalMag model by Baerenzung et al. (2020). The hyperparameters that maximize the marginal likelihood and define the prior used for constructing the model are given in Table 2. We compare ArchKalMag14k to the models ARCH10k.1 (C. Constable et al., 2016) and SHA.DIF.14k (Pavón-Carrasco et al., 2014), as both rest on a similar database and cover a similar timespan.

255

256

257

258

259

Running the inversion as described in Section 2 gives 281 sets of 440 main field and 440 secular variation coefficients together with the respective covariances, one set every 50 years. Figure 3 shows the dipole and axial quadrupole and octopole coefficients together with 95%-uncertainties and comparison models. The proposed model ArchKalMag14k shows less variation in the dipole degrees than comparable models, especially

<sup>2</sup>  $\gamma_1^0$  is the constant a priori axial dipole,  $\alpha_{\text{DP}}$  and  $\alpha_{\text{ND}}$  give the a priori scaling of the dipole and non-dipole covariance kernel respectively.  $\tau_{\text{DP}}$  and  $\tau_{\text{ND}}$  give the corresponding a priori correlation times.  $\rho$  is the scaling factor of the residual term. Note that  $\gamma_1^0$  and  $\alpha_{\bullet}$  are given at the reference radius.

**Table 2.** Prior hyperparameters for ArchKalMag14k. Note that  $\gamma_1^0$  and  $\alpha_\bullet$  are given at the reference radius. At the Earth’s surface,  $\gamma_1^0 \approx -36.19 \mu\text{T}$ .

$\gamma_1^0$ [ $\mu\text{T}$ ]	$\alpha_{\text{DP}}$ [ $\mu\text{T}$ ]	$\tau_{\text{DP}}$ [yrs.]	$\alpha_{\text{ND}}$ [ $\mu\text{T}$ ]	$\tau_{\text{ND}}$ [yrs.]	$\rho$ [ $\mu\text{T}$ ]
-426.33	28.66	183.22	111.63	316.00	3.35

260 during earlier times when data is sparse. More variation is present in the quadrupole and  
 261 octopole, with variation decreasing towards earlier times.

262 This behavior is also reflected in the power spectra. Figure 4 shows the spatial (top  
 263 row) and secular variation (bottom row) spectra for two selected epochs, one with dense  
 264 (1000 CE) and one with sparse (6000 BCE) data coverage. The blue lines show the power  
 265 spectrum as a random variable, together with the corresponding prior as a light blue dashed  
 266 line. These curves represent the non-linear transformations of the prior and posterior dis-  
 267 tribution. We also plot the power spectrum of the mean model (grey lines), i.e. the power  
 268 spectrum directly inferred from the mean coefficients. The random variable gives higher  
 269 values than the mean and comparison models, as it also includes the variance of the co-  
 270 efficients. The random variable can be compared to the prior, to determine the model  
 271 resolution, while the power spectrum of the mean is better suited for comparison to ex-  
 272 isting models. For the recent epoch, the spectrum lies between the one for ARCH10k.1  
 273 (orange) and SHA.DIF.14k (green). For the earlier epoch, more power is present in de-  
 274 grees 2 and 3 and a more rapid decrease in power is observed for the higher degrees, than  
 275 in the comparison models. For the secular variation the prior is reproduced from degree  
 276 3 on at both epochs. For the earlier epoch, the dipole secular variation power is also close  
 277 to the prior. The mean model shows less secular variation in the dipole than the com-  
 278 parison models, with more power in degrees 2 to 4. For the recent epoch, more varia-  
 279 tion is observed in the higher degrees with a more rapid decrease in power for the ear-  
 280 lier epoch, similar to the spatial spectrum.

281 Figures 5 and 6 show local curves for Paris and Hawaii respectively. Data from a  
 282 surrounding of 250km is translated to the location of prediction. Inclination and inten-  
 283 sity are translated along the corresponding axial dipoles (Merrill et al., 1996). Declina-  
 284 tions are taken as reported. The two locations were chosen because they have very dif-  
 285 ferent data coverage: Paris is covered well during recent times with a decrease in data  
 286 from 1000 BCE on and virtually no data for epochs earlier than 6000 BCE. This is re-  
 287 flected in the prediction curves, which show less variation and increasing uncertainties  
 288 for times with low data coverage. Hawaii is not as densely covered during recent times,  
 289 but due to the volcanic area, records are available over the whole timespan of the model.  
 290 Consequently, the predictions show variations during earlier times and the reported un-  
 291 certainties are smaller. The comparison models agree within the reported 95%-intervals  
 292 for both locations. For Paris, the SHA.DIF.14k model shows more variation during times  
 293 earlier than 5000 BCE and most prominently from 12000 to 8000 BCE. For Hawaii, all  
 294 models show a similar amount of variation, with SHA.DIF.14k varying slightly more and  
 295 ARCH10k.1 slightly less, especially in the intensity.

### 296 3.3 Dipole moment and location

297 During the Holocene, the geomagnetic field is dipole dominated. Therefore it is of  
 298 special interest to infer the dynamics of the dipole. Figure 7 shows the evolution of the  
 299 dipole moment. To access the dipole moment mean and standard deviation, sampling  
 300 techniques are employed. The proposed model ArchKalMag14k shows significantly less  
 301 variation in the dipole moment than comparable models. We observe some rapid vari-  
 302 ations from 1000 BCE to today, but for earlier times no rapid variations are found. In-

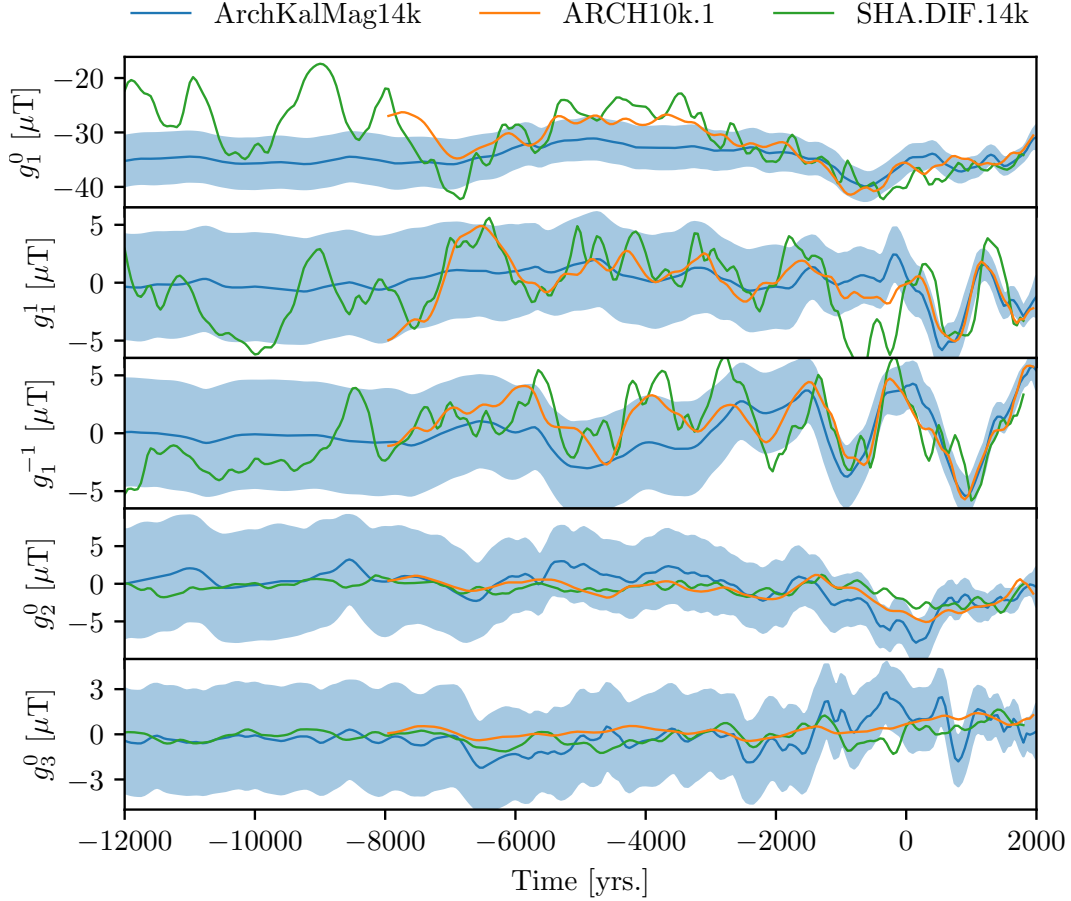


**Figure 3.** Gauss coefficients of the dipole and the axial quadru- and octopole. ArchKalMag14k is shown in blue. The shaded area covers 95%. ARCH10k.1 is shown in orange and SHA.DIF.14k in green.

303 interestingly we observe a higher dipole moment than the comparison models for the in-  
 304 terval 6000 to 2000 BCE and also from 12000 to 8000 BCE.

305 Figure 8 shows the latitude and longitude of the dipole location, together with the  
 306 angular standard deviation (Butler, 2004). The latter is inferred via sampling. In ear-  
 307 lier studies (Mauerberger et al., 2020; M. Schanner et al., 2021) we analyzed the statis-  
 308 tics of the dipole axis coordinates directly. Here we analyze the projection of the dipole  
 309 onto the sphere instead. The corresponding distribution is approximated by a von Mises-  
 310 Fisher distribution and we report the latitude and longitude of its location parameter,  
 311 instead of the mean of the marginal distributions. The advantage of performing statis-  
 312 tics on the sphere instead of considering the marginal distribution is that there is no crit-  
 313 ical point (resp. meridian). The disadvantage is that the distribution is not available in  
 314 closed form and that uncertainties can not easily be translated to latitude and longitude,  
 315 as approximations become unreliable when close to the pole (singularity in Eq. 6). Sim-  
 316 ilar to the dipole moment, the proposed model shows less variation during earlier times.  
 317 The dipole latitude shows a trend opposite to the SHA.DIF.14k model for the interval  
 318 12000 to 6000 BCE, with the geomagnetic pole being very close to the geographic one  
 319 in the beginning and a decrease in latitude towards recent times, in contrast to an in-  
 320 crease present in the SHA.DIF.14k model. The angular standard deviation (Figure 8,

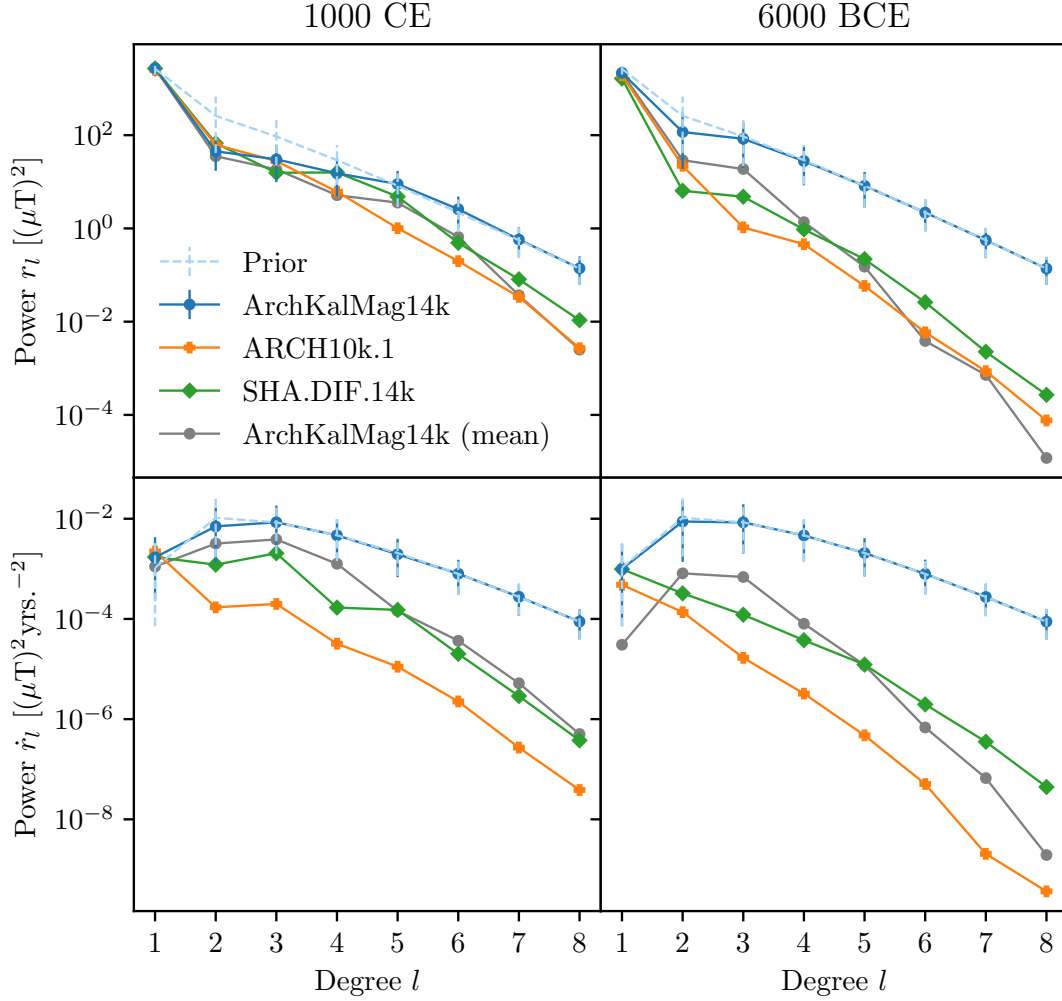


**Figure 4.** Geomagnetic main field (top) and secular variation spectra (bottom) at Earth's surface for two selected epochs. The random variable power spectrum for ArchKalMag14k is shown in blue. The errorbars report 2.5- and 97.5-percentiles, covering 95%. For comparison, the spectra of the mean model are shown in grey. The prior spectrum is shown as a light blue dashed line. ARCH10k.1 is shown in orange and SHA.DIF.14k in green. See the text for additional discussion.

321 bottom row) increases towards earlier times, as is expected from the thinning data dis-  
 322 tribution.

323 **3.4 South Atlantic anomaly**

324 To conclude the results, we present investigations of the South Atlantic Anomaly  
 325 (SAA). The SAA is a region of low field intensity, that has been linked to reverse flux  
 326 patches at the CMB during recent times (e.g. Terra-Nova et al., 2017). We compare the  
 327 appearance and evolution of the SAA as predicted by ArchKalMag14k to other studies  
 328 (Hartmann & Pacca, 2009; Campuzano et al., 2019). We do not follow the kernel-based  
 329 approach of Terra-Nova et al. (2017), but investigate maps of the magnetic fields radial  
 330 component at the CMB. In general, due to the projection into the Earth's interior, un-  
 331 certainties at the CMB are so large that reverse flux in the mean is not resolved reliably

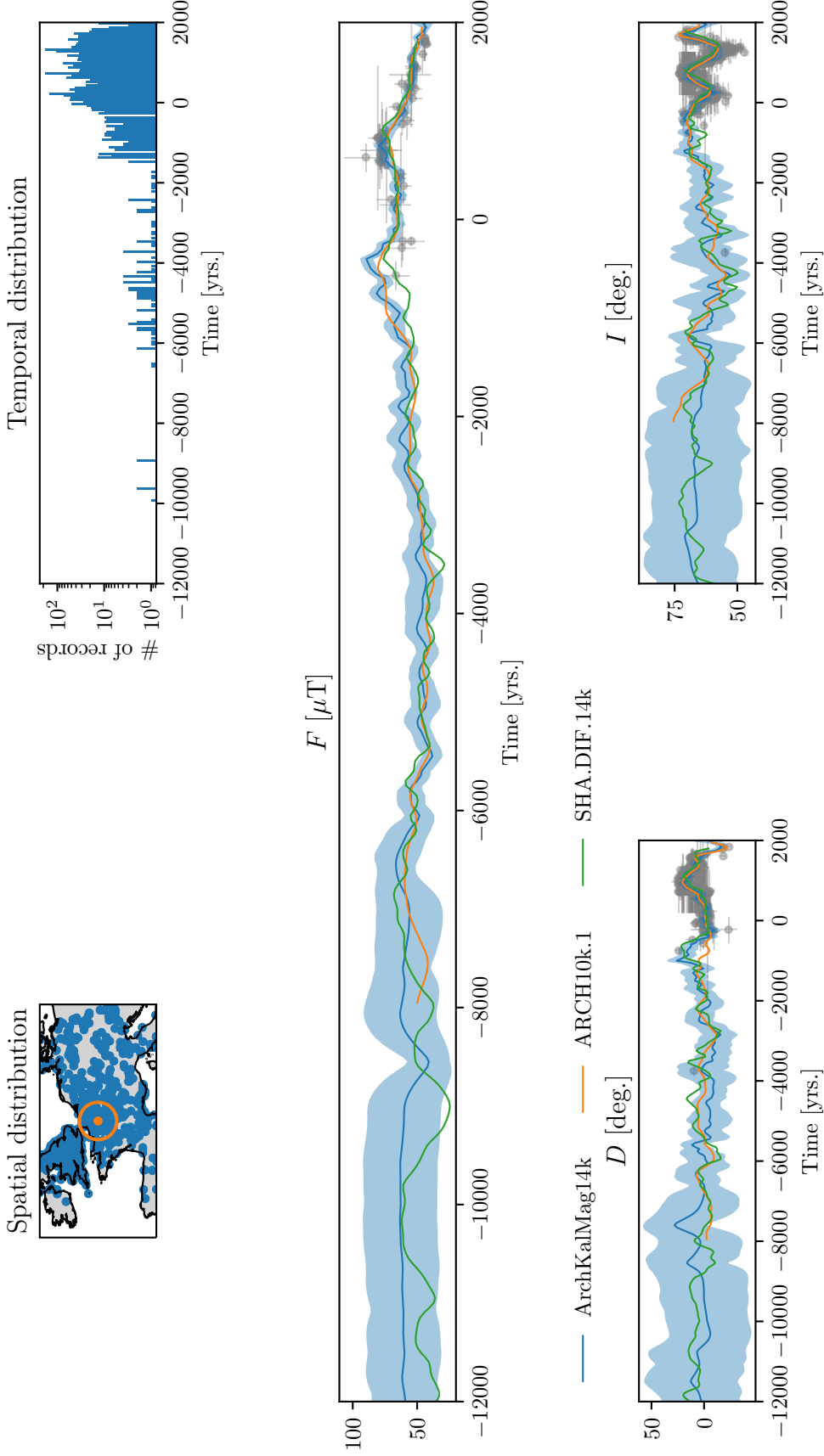


**Figure 5.** Local predictions of intensity  $F$ , declination  $D$  and inclination  $I$  for Paris. ArchKalMag14k is shown in blue. The shaded area covers 95%. ARCH10k.1 is shown in orange and SHA.DIF.14k in green. In the top row, the spatial and temporal distribution of the surrounding are shown. Data in the orange ellipse (250km radius) are translated to the location of prediction (orange dot) and shown as gray dots. Horizontal and vertical gray bars indicate the one sigma temporal and field component data uncertainties, respectively. The temporal distribution includes all data visible in the left plot.

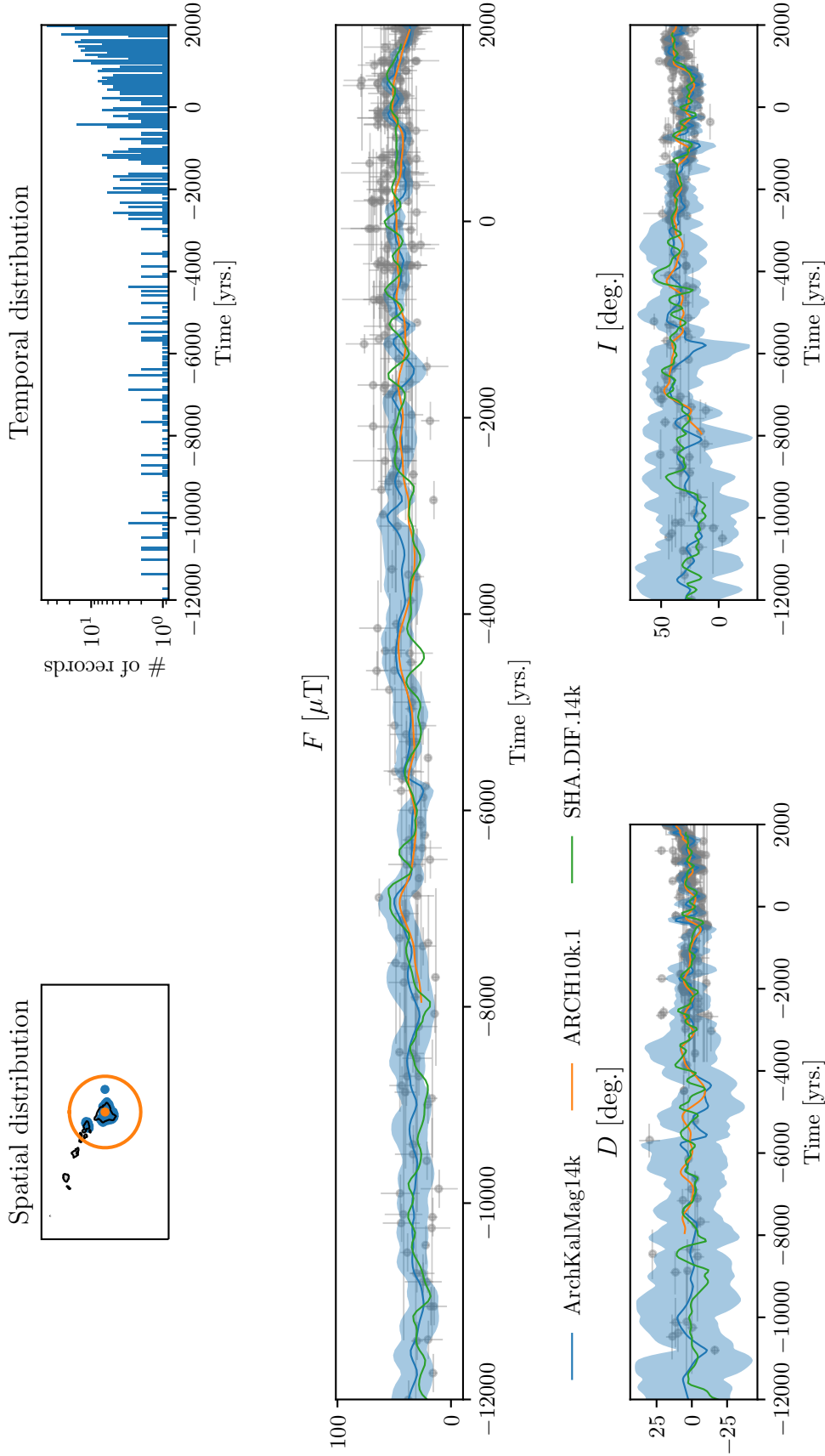


**Figure 6.** Local predictions of intensity  $F$ , declination  $D$  and inclination  $I$  for Hawaii. ArchKalmag14k is shown in blue. The shaded area covers 95%. ARCH10k.1 is shown in orange and SHA.DIF.14k in green. In the top row, the spatial and temporal distribution of the surrounding are shown. Data in the orange ellipse (250km radius) are translated to the location of prediction (orange dot) and shown as gray dots. Horizontal and vertical gray bars indicate the one sigma temporal and field component data uncertainties, respectively. The temporal distribution includes all data visible in the left plot.

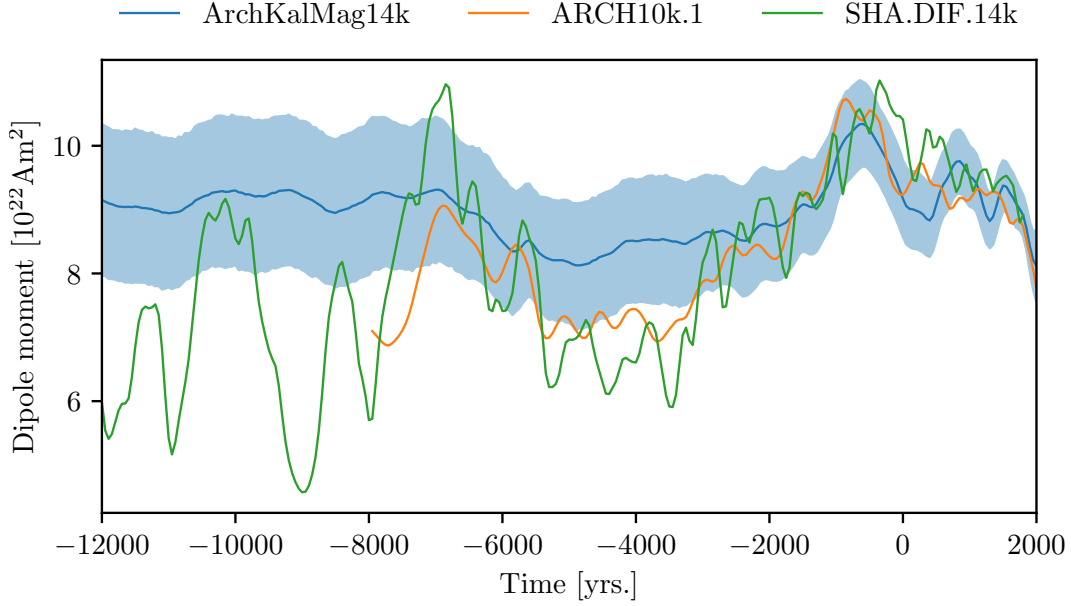


**Figure 7.** Dipole moment of the geomagnetic field. ArchKalMag14k is shown in blue. The shaded area covers 95%. ARCH10k.1 is shown in orange and SHA.DIF.14k in green. Mean and standard deviation of ArchKalMag14k are inferred from sampling. This sampling is the reason for the small scale noise in the blue curve and area.

332 and more data and future work are required to confirm these findings. We consider the  
333 projections qualitatively nevertheless.

334 We find a region of field intensity lower than  $32 \mu\text{T}$  emerging close to the tip of Brazil  
335 at 1200 CE. Reverse flux is present to the north and a patch of reverse flux is located  
336 directly south of the region. Together with this patch, the region of low intensity rapidly  
337 moves south-eastward to the coast of today's Namibia, where it is located in 1300 CE  
338 (Fig. 9, b)). This contrasts the findings of Campuzano et al. (2019), where the low in-  
339 tensity region emerges approximately 100 years earlier close to Madagascar. The SAA  
340 then extends to the West and slightly to the East, with the center drifting westward un-  
341 til 1500 CE, back to the origin of the region. From there it moves East and constricts  
342 at the coast of today's Namibia, almost disappearing at 1650 CE. This dynamic is also  
343 not present in SHA.WQ.2k by Campuzano et al. (2019), where the SAA persists at the  
344 coast of Namibia and does not decrease in size. The described evolution precedes the dy-  
345 namics found by Hartmann and Pacca (2009). The subsequent westward drift of the low  
346 intensity region generally agrees with their findings and the findings of Campuzano et  
347 al. (2019) within the uncertainties.

348 Further, we find a low field intensity region emerging in 250 BCE west of today's  
349 Peru. It drifts south-eastward and in 500 CE merges with a second low field intensity  
350 region that emerges around 400 CE North-East of Madagascar. Both anomalies are ac-  
351 companied by reverse flux in the Southern hemisphere. The joint low intensity region  
352 continues to drift eastward and shrinks, persisting until 900 CE. Campuzano et al. (2019)  
353 find a low intensity field region emerging at the coast of Namibia at 175 CE. In their find-  
354 ings the earlier anomaly is static and grows until 500 CE. It then shrinks and disappears  
355 at 700 CE, earlier than in our findings.

356 Low intensity regions around the equator are present from the beginning of the model  
357 timespan on, but uncertainties are too large to reliably interpret their appearance. First

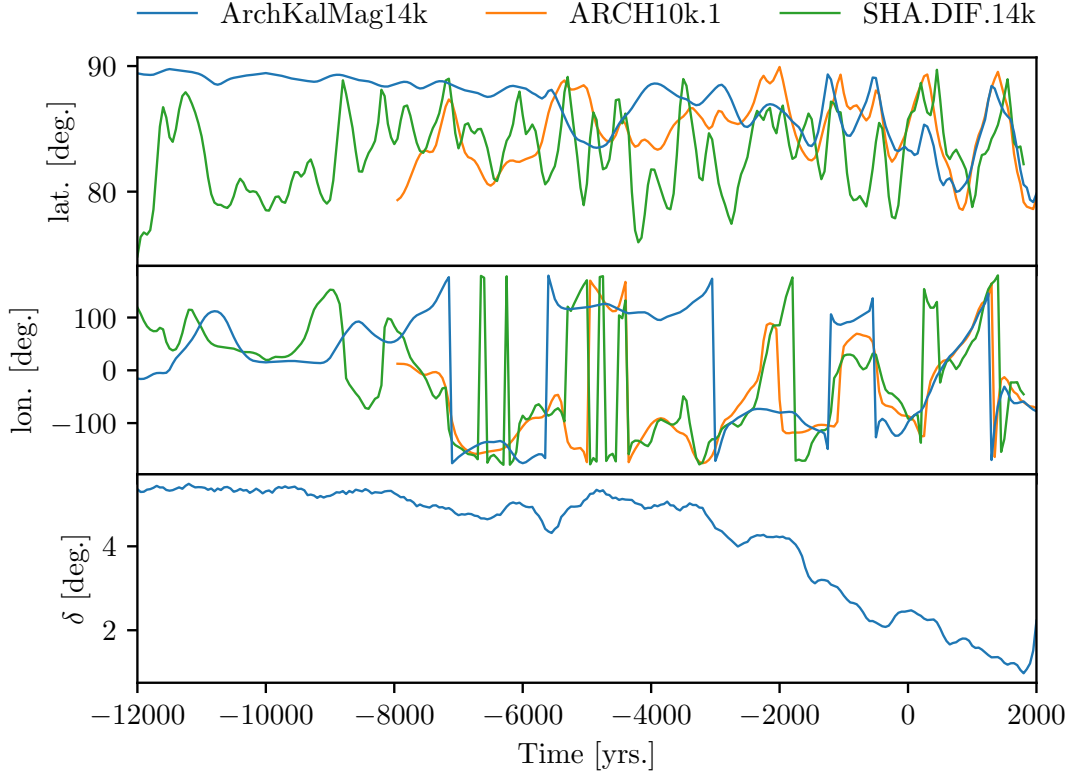


**Figure 8.** Latitude (top) and longitude (middle) of the geomagnetic dipole axis. ArchKalMag14k is shown in blue. ARCH10k.1 is shown in orange and SHA.DIF.14k in green. The bottom plot shows the angular standard deviation  $\delta$  (Butler, 2004) for ArchKalMag14k, which is inferred from sampling. This sampling is the reason for the small scale noise in earlier times.

358 reliable hints on a low intensity field region in the Indian ocean are present around 3000  
 359 BCE, with the region drifting eastward and a second low intensity region appearing over  
 360 the Northern part of South America at 2600 BCE. The anomaly in the Indian ocean dis-  
 361 appears at 2200 BCE. The one above South America is accompanied by pronounced re-  
 362 verse flux, although during these epochs uncertainties at the CMB are even higher than  
 363 during recent times and caution has to be taken when interpreting the results. The anomaly  
 364 persists over South America, extends until 1500 BCE (Fig. 9, a)) and vanishes in 1200  
 365 BCE.

366 Overall the model shows low field intensity anomalies, accompanied by reverse flux,  
 367 emerging and vanishing regularly, with a cycle in the order of 1000 years. An animation  
 368 of the field at the Earth's surface and the CMB can be found with the supplementary  
 369 material.

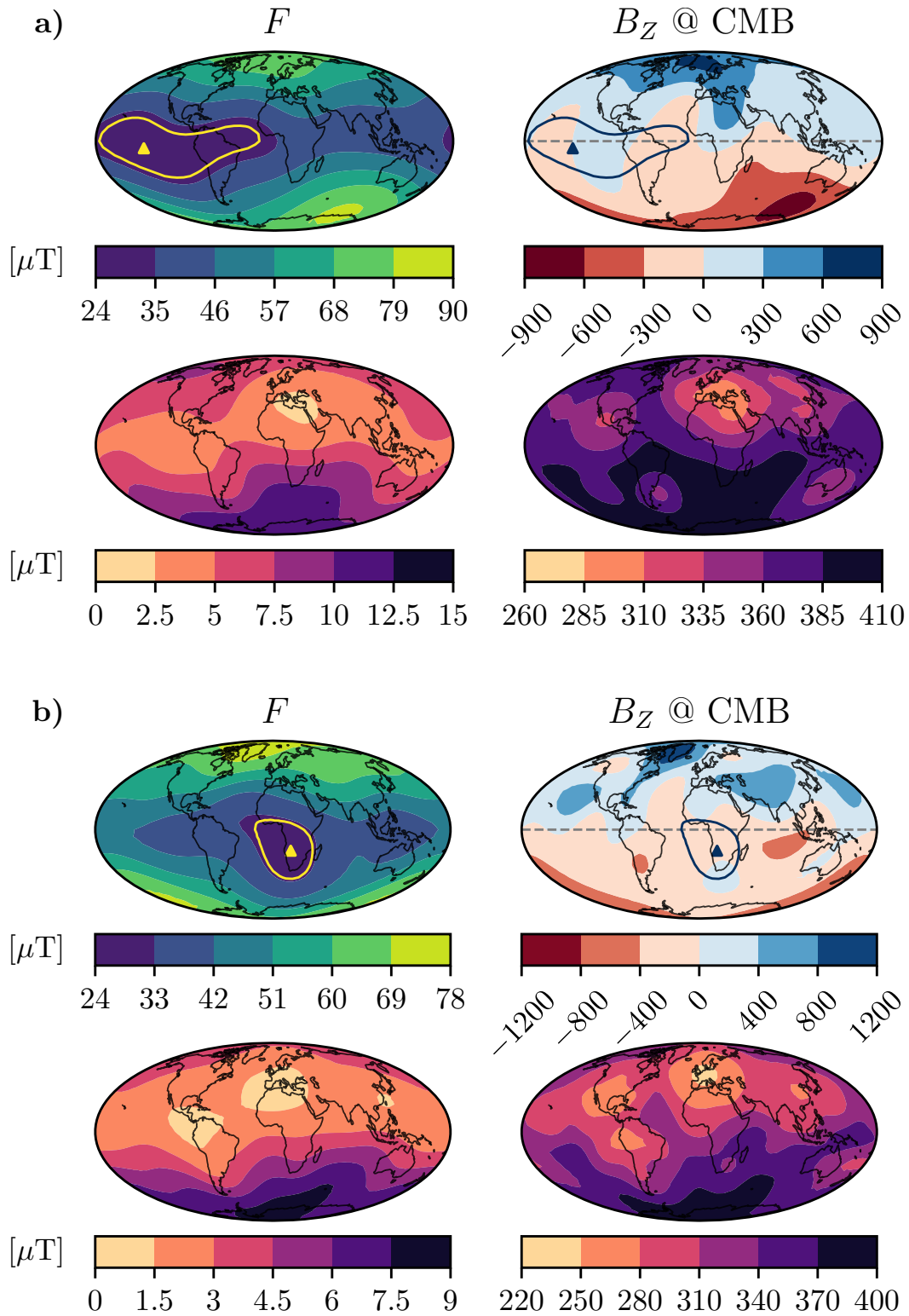


**Figure 9.** The South Atlantic Anomaly (SAA). The top rows show the field intensity at the Earth’s surface and the magnetic field radial component (downwards). The bottom rows show the respective standard deviation. a) is for the year 1500 BCE and b) for 1300 CE. The yellow triangles indicate the location of lowest field intensity. The yellow contour line corresponds to a field value of  $32 \mu\text{T}$ . For reference, both location of lowest intensity and contour are also shown in the CMB plots in blue.

## 4 Discussion

In the preceding section we proposed the new global geomagnetic field model ArchKalMag14k and presented its features. The local predictions give a reasonable representation of the underlying archeomagnetic data and agree with comparison models within the uncertainties. If no data is present, local curves show significantly less variation than the compared models. Low order, global scale degrees are only resolved if a sufficient amount of data is present. In this case, local predictions for remote locations also show rapid variations and uncertainties are relatively small (see the local predictions for the Indian ocean in the supplementary material). If the data cannot resolve the global scales, the prior is reproduced, which is evident from local curves with no data coverage (Fig. 5) and the analysis of the dipole itself (Figs. 7 and 8). For times earlier than 6000 BCE, the axial dipole varies only slightly around the prior mean value of approx.  $-36.19 \mu\text{T}$  (Fig. 3, top row). Nevertheless, local variations are resolved, if supported by the data (Fig. 6, especially the dip in declination at 11000 BCE). Spatial power spectra provide insight on the resolution of the model on global scales. From a comparison of the spectra to the respective prior it is evident, that for recent times information up to degree 6 is obtained, while for the earlier times the prior is reproduced already at degree 3 (Fig. 4, top row). An investigation of low intensity field regions reproduces the emergence and evolution of the South Atlantic Anomaly (SAA) in recent times (from 1600 CE on), while the preceding dynamics differ from other studies (Campuzano et al., 2019). Low intensity field regions can be resolved from 3000 BCE on. Although uncertainties at the CMB are large, hints for reverse flux patches associated with these field anomalies are found. A detailed evaluation relating these patches to the anomalies, e.g. based on kernels (Terra-Nova et al., 2017) remains to be done and more data are needed to reduce the uncertainties.

In contrast to other recently proposed Bayesian models (Hellio & Gillet, 2018; Nilsson & Suttie, 2021), most prior parameters of ArchKalMag14k are inferred from the data via maximization of the log marginal likelihood. As the marginal likelihood drops off quickly around the maximum, we did not perform an integration as proposed in the last study (M. Schanner et al., 2021). The a priori assumption of a constant axial dipole may lead to an underestimation of uncertainties in the dipole degrees, moment and location, as the prior mean is constrained well by data from recent times and variations during earlier times are considered around this fixed, constant value. Using only part of the recent records to create a dataset that is more homogeneous in time may improve this, but leads to other complications as hyperparameters become less constrained and harder to determine, when fewer records are available. Artificially increasing the a priori dipole variance leads to more variation around the constant mean during earlier times, but also to higher posterior uncertainties and the model we propose lies well within these. Two scenarios are reasonable, to explain the absence of variations during earlier times in our model. Either the statistical properties (and thus the underlying processes) of the EMF changed during the Holocene, some time around 3000 BCE. This is supported by a visual inspection of the top row in Figure 3 and Figure 7. Or the data do not contain enough information to recover the global dynamics of the field, which is supported by the findings of the validation section. Additional data, e.g. from sediments may help recovering the actual field dynamics, but require significant adaption of the modeling method.

## 5 Conclusions

This study proposes a new global geomagnetic model for the Holocene, called ArchKalMag14k. We modified the algorithms suggested in earlier works (Mauerberger et al., 2020; M. Schanner et al., 2021) to be applicable to the archeomagnetic database. The inversion is sequentialized by means of a Kalman-filter (Kalman, 1960; Baerenzung et al., 2020). The resulting model consists of sets of Gauss coefficients, secular variations and covariances, stored every 50 years. The model can be reproduced by code that is publicly available (<https://sec23.git-pages.gfz-potsdam.de/korte/paleokalmag/>) or

422 is provided upon request. ArchKalMag14k can be imported by pymagglobal (M. A. Schanner  
423 et al., 2020), so that feature analysis is straight-forward.

424 The central result of this study is that for times earlier than 6000 BCE the cur-  
425 rent database of thermoremanent records alone does not contain enough information to  
426 construct global models. For times earlier than 6000 BCE, ArchKalMag14k reproduces  
427 the prior on a global scale and only local variations are resolved. Existing models may  
428 further overconfidently report variations during times later than 6000 BCE, as local vari-  
429 ations that are resolved by higher degrees in ArchKalMag14k result in variations of the  
430 large scale dipole in existing models.

431 The next step is to extend and adapt the modeling framework to incorporate sed-  
432 iment records. As the recent study by (Nilsson & Suttie, 2021) shows, this requires sig-  
433 nificant modifications due to aspects of the sedimentation process and the respective sta-  
434 tistical implications.

### 435 Acknowledgments

436 This work was funded by the Deutsche Forschungsgemeinschaft (DFG, German Research  
437 Foundation), grant 388291411. M. Schanner performed theoretical and conceptual work,  
438 with support from both co-authors. The manuscript was assembled by M. Schanner, with  
439 support from all co-authors. Software development and data processing was conducted  
440 by M. Schanner. The work and findings were supervised by M. Korte and M. Holschnei-  
441 der.

442 Special thanks go to A. N. Mahgoub for sharing his experience and knowledge on  
443 records from Mexico, to J. Baerenzung for sharing insights on the Kalman filter algo-  
444 rithm and to S. Mauerberger for valuable discussions on different aspects of this study.

445 The dataset used in this study is a slight variation of all records from the archae-  
446 ological and volcanic database from GEOMAGIA v3.4 (Brown et al., 2015) with ages  
447 between 12000 BCE and 2000 CE. Some of the records from Mexico contain wrong ages  
448 (Mahgoub, pers. comm.), so they have been altered or removed, if no better estimate was  
449 available. A list of altered records is available with the supplementary material. All re-  
450 sults were produced using a python implementation of the discussed algorithm, which  
451 is publicly available at <https://sec23.git-pages.gfz-potsdam.de/korte/paleokalmag/>.

### 452 References

- 453 Baerenzung, J., Holschneider, M., Wicht, J., Lesur, V., & Sanchez, S. (2020).  
454 The kalmag model as a candidate for IGRF-13. *Earth Planets Space*, 72,  
455 163. Retrieved from [https://earth-planets-space.springeropen.com/](https://earth-planets-space.springeropen.com/articles/10.1186/s40623-020-01295-y)  
456 [articles/10.1186/s40623-020-01295-y](https://earth-planets-space.springeropen.com/articles/10.1186/s40623-020-01295-y) doi: [https://doi.org/10.1186/](https://doi.org/10.1186/s40623-020-01295-y)  
457 [s40623-020-01295-y](https://doi.org/10.1186/s40623-020-01295-y)
- 458 Brown, M. C., Donadini, F., Nilsson, A., Panovska, S., Frank, U., Korhonen, K.,  
459 ... Constable, C. G. (2015). Geomag50.v3: 2. a new paleomagnetic  
460 database for lake and marine sediments. *Earth, Planets and Space*, 67(1),  
461 70. Retrieved from <https://doi.org/10.1186/s40623-015-0233-z> doi:  
462 [10.1186/s40623-015-0233-z](https://doi.org/10.1186/s40623-015-0233-z)
- 463 Butler, R. F. (2004). *Paleomagnetism*. Blackwell Scientific Publications. (Electronic  
464 edition)
- 465 Campuzano, S., Gómez-Paccard, M., Pavón-Carrasco, F., & Osete, M. (2019).  
466 Emergence and evolution of the south atlantic anomaly revealed by the  
467 new paleomagnetic reconstruction shawq2k. *Earth and Planetary Science*  
468 *Letters*, 512, 17-26. Retrieved from <https://www.sciencedirect.com/>

- 469 science/article/pii/S0012821X19300822 doi: [https://doi.org/10.1016/](https://doi.org/10.1016/j.epsl.2019.01.050)  
 470 j.epsl.2019.01.050
- 471 Constable, C., & Korte, M. (2015). 5.09 - centennial- to millennial-scale geomagnetic  
 472 field variations. In G. Schubert (Ed.), *Treatise on geophysics (second edition)*  
 473 (Second Edition ed., p. 309-341). Oxford: Elsevier. Retrieved from [https://](https://www.sciencedirect.com/science/article/pii/B9780444538024001032)  
 474 [www.sciencedirect.com/science/article/pii/B9780444538024001032](https://www.sciencedirect.com/science/article/pii/B9780444538024001032)  
 475 doi: <https://doi.org/10.1016/B978-0-444-53802-4.00103-2>
- 476 Constable, C., Korte, M., & Panovska, S. (2016). Persistent high paleosecular varia-  
 477 tion activity in southern hemisphere for at least 10 000 years. *Earth and Plane-*  
 478 *tary Science Letters*, *453*, 78 - 86. doi: 10.1016/j.epsl.2016.08.015
- 479 Constable, C. G., Johnson, C. L., & Lund, S. P. (2000). Global geomagnetic field  
 480 models for the past 3000 years: transient or permanent flux lobes? *Phil.*  
 481 *Trans. R. Soc. Lond. A*, *358*, 991-1008.
- 482 Constable, C. G., & Parker, R. L. (1988). Statistics of the geomagnetic secular  
 483 variation for the past 5 m.y. *Journal of Geophysical Research: Solid Earth*,  
 484 *93*(B10), 11569-11581. doi: 10.1029/JB093iB10p11569
- 485 Gillet, N., Jault, D., Finlay, C. C., & Olsen, N. (2013). Stochastic modeling of the  
 486 Earth's magnetic field: Inversion for covariances over the observatory era. *Geo-*  
 487 *chemistry, Geophysics, Geosystems*, *14*(4), 766-786. Retrieved from [https://](https://agupubs.onlinelibrary.wiley.com/doi/abs/10.1002/ggge.20041)  
 488 [agupubs.onlinelibrary.wiley.com/doi/abs/10.1002/ggge.20041](https://agupubs.onlinelibrary.wiley.com/doi/abs/10.1002/ggge.20041) doi: 10  
 489 .1002/ggge.20041
- 490 Hartmann, G. A., & Pacca, I. G. (2009). Time evolution of the south at-  
 491 lantic magnetic anomaly. *Anais da Academia Brasileira de Ciências*,  
 492 *81*, 243 - 255. Retrieved from [http://www.scielo.br/scielo.php](http://www.scielo.br/scielo.php?script=sci_arttext&pid=S0001-37652009000200010&nrm=iso)  
 493 [?script=sci\\_arttext&pid=S0001-37652009000200010&nrm=iso](http://www.scielo.br/scielo.php?script=sci_arttext&pid=S0001-37652009000200010&nrm=iso) doi:  
 494 10.1590/S0001-37652009000200010
- 495 Hellio, G., & Gillet, N. (2018). Time-correlation-based regression of the geomag-  
 496 netic field from archeological and sediment records. *Geophysical Journal Inter-*  
 497 *national*, *214*(3), 1585-1607. doi: 10.1093/gji/ggy214
- 498 Hellio, G., Gillet, N., Bouligand, C., & Jault, D. (2014). Stochastic modelling of  
 499 regional archaeomagnetic series. *Geophysical Journal International*, *199*, 931-  
 500 943. doi: 10.1093/gji/ggu303
- 501 Holschneider, M., Lesur, V., Mauerberger, S., & Baerenzung, J. (2016). Correlation-  
 502 based modeling and separation of geomagnetic field components. *Journal*  
 503 *of Geophysical Research: Solid Earth*, *121*(5), 3142-3160. doi: 10.1002/  
 504 2015JB012629
- 505 Jackson, A., & Finlay, C. (2015). Geomagnetic secular variation and its applications  
 506 to the core. In G. Schubert (Ed.), *Treatise on geophysics* (2nd ed., Vol. 5, pp.  
 507 137-184). United Kingdom: Elsevier. doi: 10.1016/B978-0-444-53802-4.00099  
 508 -3
- 509 Jackson, A., Jonkers, A., & Walker, M. (2000). Four centuries of geomagnetic  
 510 secular variation from historical records. *Philosophical Transactions of the*  
 511 *Royal Society of London A: Mathematical, Physical and Engineering Sciences*,  
 512 *358*(1768), 957-990. doi: 10.1098/rsta.2000.0569
- 513 Kalman, R. E. (1960). A new approach to linear filtering and prediction prob-  
 514 lems. *Transactions of the ASME-Journal of Basic Engineering*, *82*(Series D),  
 515 35-45.
- 516 King, D. E. (2009). Dlib-ml: A machine learning toolkit. *Journal of Machine Learn-*  
 517 *ing Research*, *10*, 1755-1758.
- 518 King, D. E. (2017). *A global optimization algorithm worth using*. [http://blog.dlib](http://blog.dlib.net/2017/12/a-global-optimization-algorithm-worth.html)  
 519 [.net/2017/12/a-global-optimization-algorithm-worth.html](http://blog.dlib.net/2017/12/a-global-optimization-algorithm-worth.html). (Accessed:  
 520 2020-07-07)
- 521 Korte, M., & Constable, C. G. (2003). Continuous global geomagnetic field models  
 522 for the past 3000 years. *Phys. Earth Planet. Interiors*, *140*, 73-89.
- 523 Korte, M., Donadini, F., & Constable, C. (2009). Geomagnetic field for 0-3ka: 2.

- 524 a new series of time-varying global models. *Geochem. Geophys. Geosys.*, *10*,  
525 *Q06008*, doi:10.1029/2008GC002297.
- 526 Korte, M., Genevey, A., Constable, C. G., Frank, U., & Schnepp, E. (2005). Con-  
527 tinuous geomagnetic field models for the past 7 millennia: 1. a new global  
528 data compilation. *Geochemistry, Geophysics, Geosystems*, *6*(2). doi:  
529 <https://doi.org/10.1029/2004GC000800>
- 530 Licht, A., Hulot, G., Gallet, Y., & Thébault, E. (2013). Ensembles of low degree  
531 archeomagnetic field models for the past three millennia. *Physics of the Earth  
532 and Planetary Interiors*, *224*, 38 - 67. doi: 10.1016/j.pepi.2013.08.007
- 533 Mauerberger, S., Schanner, M., Korte, M., & Holschneider, M. (2020). Correlation  
534 based snapshot models of the archeomagnetic field. *Geophysical Journal Inter-  
535 national*. Retrieved from <https://doi.org/10.1093/gji/ggaa336> (ggaa336)  
536 doi: 10.1093/gji/ggaa336
- 537 McHutchon, A., & Rasmussen, C. E. (2011). Gaussian process training with in-  
538 put noise. In J. Shawe-Taylor, R. S. Zemel, P. L. Bartlett, F. Pereira, &  
539 K. Q. Weinberger (Eds.), *Advances in neural information processing systems*  
540 *24* (pp. 1341–1349). Curran Associates, Inc.
- 541 Merrill, R. T., McElhinny, M. W., & McFadden, P. L. (1996). *The magnetic field  
542 of the earth: Paleo-magnetism, the core, and the deep mantle*. Academic Press,  
543 San Diego.
- 544 Nilsson, A., & Suttie, N. (2021). Probabilistic approach to geomagnetic field  
545 modelling of data with age uncertainties and post-depositional magneti-  
546 sations. *Physics of the Earth and Planetary Interiors*, *317*, 106737. Re-  
547 trieved from [https://www.sciencedirect.com/science/article/pii/  
548 S0031920121000959](https://www.sciencedirect.com/science/article/pii/S0031920121000959) doi: <https://doi.org/10.1016/j.pepi.2021.106737>
- 549 Pavón-Carrasco, F. J., Osete, M. L., Torta, J. M., & De Santis, A. (2014). A  
550 geomagnetic field model for the holocene based on archaeomagnetic and  
551 lava flow data. *Earth and Planetary Science Letters*, *388*, 98-109. Re-  
552 trieved from [https://www.sciencedirect.com/science/article/pii/  
553 S0012821X13006869](https://www.sciencedirect.com/science/article/pii/S0012821X13006869) doi: <https://doi.org/10.1016/j.epsl.2013.11.046>
- 554 Piper, J. D. A. (1989). Paleomagnetism. In J. A. Jacobs (Ed.), *Geomagnetism*  
555 (Vol. 3, p. 31-61). Academic Press.
- 556 Rasmussen, C., & Williams, C. (2006). *Gaussian processes for machine learning*.  
557 MIT Press, Cambridge, MA.
- 558 Rauch, H. E., Tung, F., & Striebel, C. T. (1965). Maximum likelihood estimates of  
559 linear dynamic systems. *AIAA Journal*, *3*(8), 1445-1450. doi: 10.2514/3.3166
- 560 Ropp, G., Lesur, V., Baerenzung, J., & Holschneider, M. (2020). Sequential  
561 modelling of the Earth’s core magnetic field. *Earth Planets Space*, *72*,  
562 153. Retrieved from [https://earth-planets-space.springeropen.com/  
563 articles/10.1186/s40623-020-01230-1](https://earth-planets-space.springeropen.com/articles/10.1186/s40623-020-01230-1) doi: [https://doi.org/10.1186/  
564 s40623-020-01230-1](https://doi.org/10.1186/s40623-020-01230-1)
- 565 Schanner, M., Mauerberger, S., Korte, M., & Holschneider, M. (2021). Correlation  
566 based time evolution of the archeomagnetic field. *Journal of Geophysical Re-  
567 search: Solid Earth*, *126*(7), e2020JB021548. Retrieved from [https://agupubs  
568 .onlinelibrary.wiley.com/doi/abs/10.1029/2020JB021548](https://agupubs.onlinelibrary.wiley.com/doi/abs/10.1029/2020JB021548) doi: [https://  
569 doi.org/10.1029/2020JB021548](https://doi.org/10.1029/2020JB021548)
- 570 Schanner, M. A., Mauerberger, S., & Korte, M. (2020). *pymagglobal - python in-  
571 terface for global geomagnetic field models*. Potsdam: GFZ Data Services. doi:  
572 <https://doi.org/10.5880/GFZ.2.3.2020.005>
- 573 Senftleben, R. (2019). *Earth’s magnetic field over the last 1 000 years* (Unpublished  
574 doctoral dissertation). University of Potsdam.
- 575 Suttie, N., & Nilsson, A. (2019). Archaeomagnetic data: The propagation of an er-  
576 ror. *Physics of the Earth and Planetary Interiors*, *289*, 73 - 74. doi: 10.1016/  
577 j.pepi.2019.02.008
- 578 Terra-Nova, F., Amit, H., Hartmann, G. A., Trindade, R. I., & Pinheiro, K. J.

579 (2017). Relating the south atlantic anomaly and geomagnetic flux  
580 patches. *Physics of the Earth and Planetary Interiors*, 266, 39-53. Re-  
581 trieved from [https://www.sciencedirect.com/science/article/pii/](https://www.sciencedirect.com/science/article/pii/S0031920116302205)  
582 S0031920116302205 doi: <https://doi.org/10.1016/j.pepi.2017.03.002>

# Supporting Information for "ArchKalMag14k: A Kalman-filter based global geomagnetic model for the Holocene"

M. Schanner<sup>1</sup>, M. Korte<sup>1</sup>, M. Holschneider<sup>2</sup>

<sup>1</sup>German Research Centre for Geosciences GFZ, Section 2.3, Potsdam, Germany

<sup>2</sup>Applied Mathematics, University of Potsdam, Potsdam, Germany

## Contents of this file

1. Figures S1 to S4
2. Table S1

## Additional Supporting Information (Files uploaded separately)

1. Captions for Movie S1

## Introduction

This supplementary material provides validation plots for additional coefficients in Figure S1, a comparison of the model coefficients with the prior in Figure S2 and local field predictions at two additional locations in Figures S3 and S4. Table S1 contains a list of changes made to the GEOMAGIA v.3.4 dataset (Brown et al., 2015). A separately available Movie S1 shows the evolution of the geomagnetic field intensity at the Earth's surface and of the radial component (downwards) at the core mantle boundary, together with respective uncertainties.

---

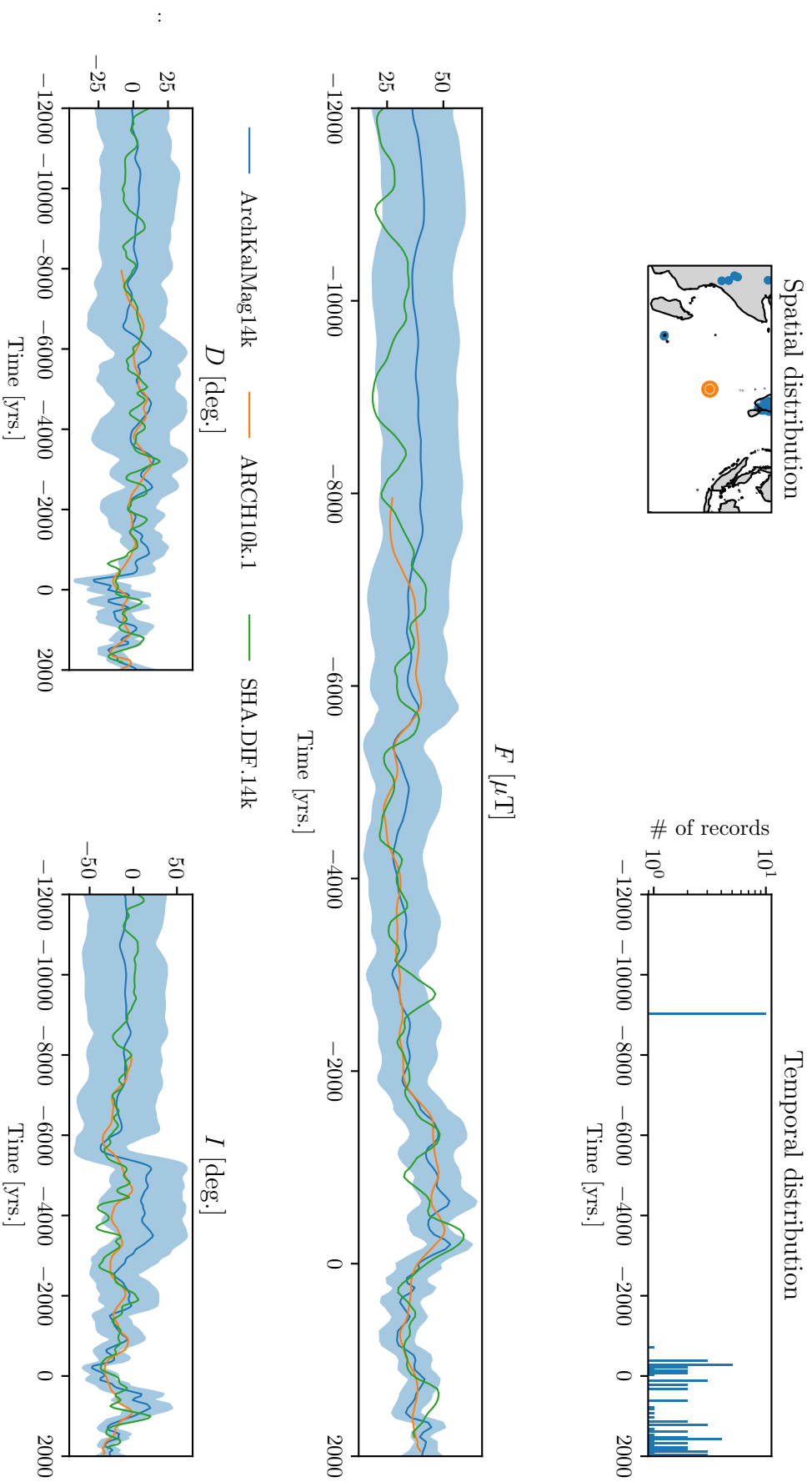


**Figure S3.** Local predictions of intensity  $F$ , declination  $D$  and inclination  $I$  for the Indian Ocean. ArchKalmag14k is shown in blue. The shaded area covers 95%. ARCH10k.1 is shown in orange and SHA.DIF.14k in green. In the top row, the spatial and temporal distribution of the surrounding are shown. Data in the orange ellipse (250km radius) are translated to the location of prediction (orange dot) and shown as gray dots. Horizontal and vertical gray bars indicate the one sigma temporal and field component data uncertainties, respectively. The temporal distribution includes all data visible in the left plot.

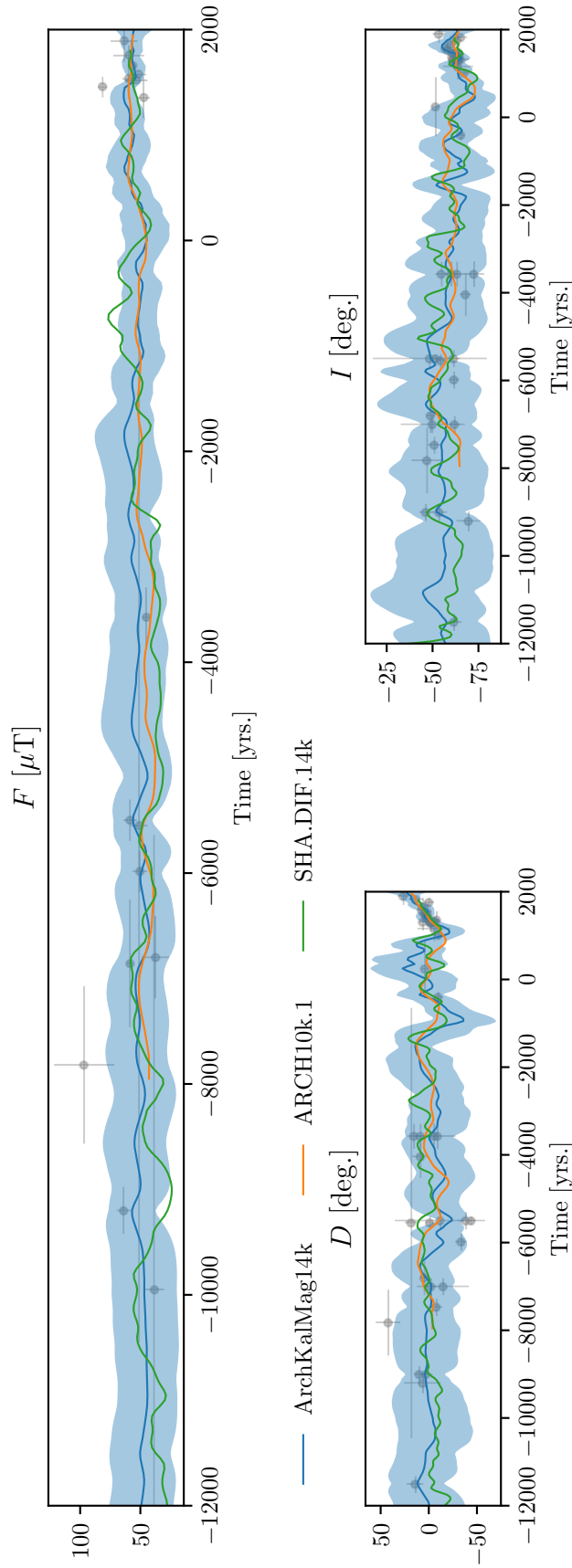
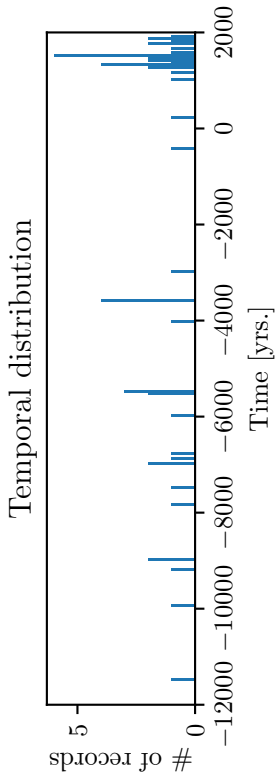
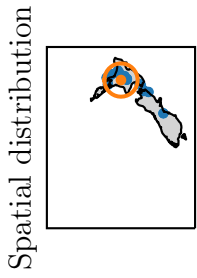


**Figure S4.** Local predictions of intensity  $F$ , declination  $D$  and inclination  $I$  for New Zealand. ArchKalMag14k is shown in blue. The shaded area covers 95%. ARCH10k.1 is shown in orange and SHA.DIF.14k in green. In the top row, the spatial and temporal distribution of the surrounding are shown. Data in the orange ellipse (250km radius) are translated to the location of prediction (orange dot) and shown as gray dots. Horizontal and vertical gray bars indicate the one sigma temporal and field component data uncertainties, respectively. The temporal distribution includes all data visible in the left plot.

**Movie S1.** Evolution of the geomagnetic field intensity at the Earth's surface (left) and of the radial component (downwards, right) at the core mantel boundary, together with respective uncertainties. The time interval of 50 years corresponds to the full resolution of ArchKalMag14k. Note, that the scales change during the movie. The yellow triangle indicates the location of lowest field intensity. The yellow contour line corresponds to a field value of  $32 \mu\text{T}$ . For reference, both location of lowest intensity and contour are also shown in the CMB plots in blue.

## References

- Brown, M. C., Donadini, F., Nilsson, A., Panovska, S., Frank, U., Korhonen, K., ...  
Constable, C. G. (2015). Geomag50.v3: 2. a new paleomagnetic database for lake and marine sediments. *Earth, Planets and Space*, *67*(1), 70. Retrieved from <https://doi.org/10.1186/s40623-015-0233-z> doi: 10.1186/s40623-015-0233-z

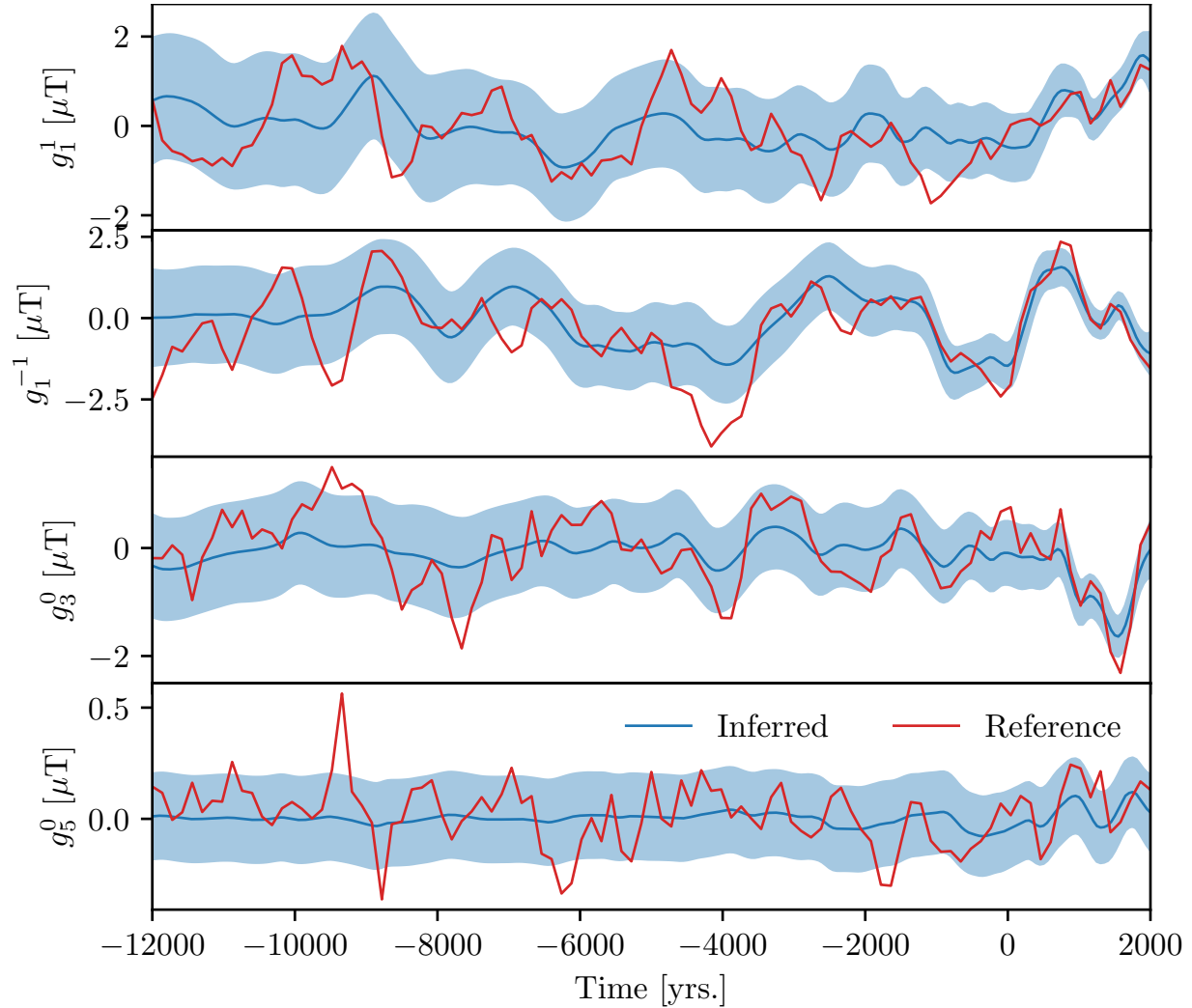


**Figure S1.** Additional dipole and higher order coefficients of the synthetic model, together with the corresponding inferred ones from the proposed inversion. The inferred (blue) and reference curves (red) agree within the 95%-region shown in light blue.

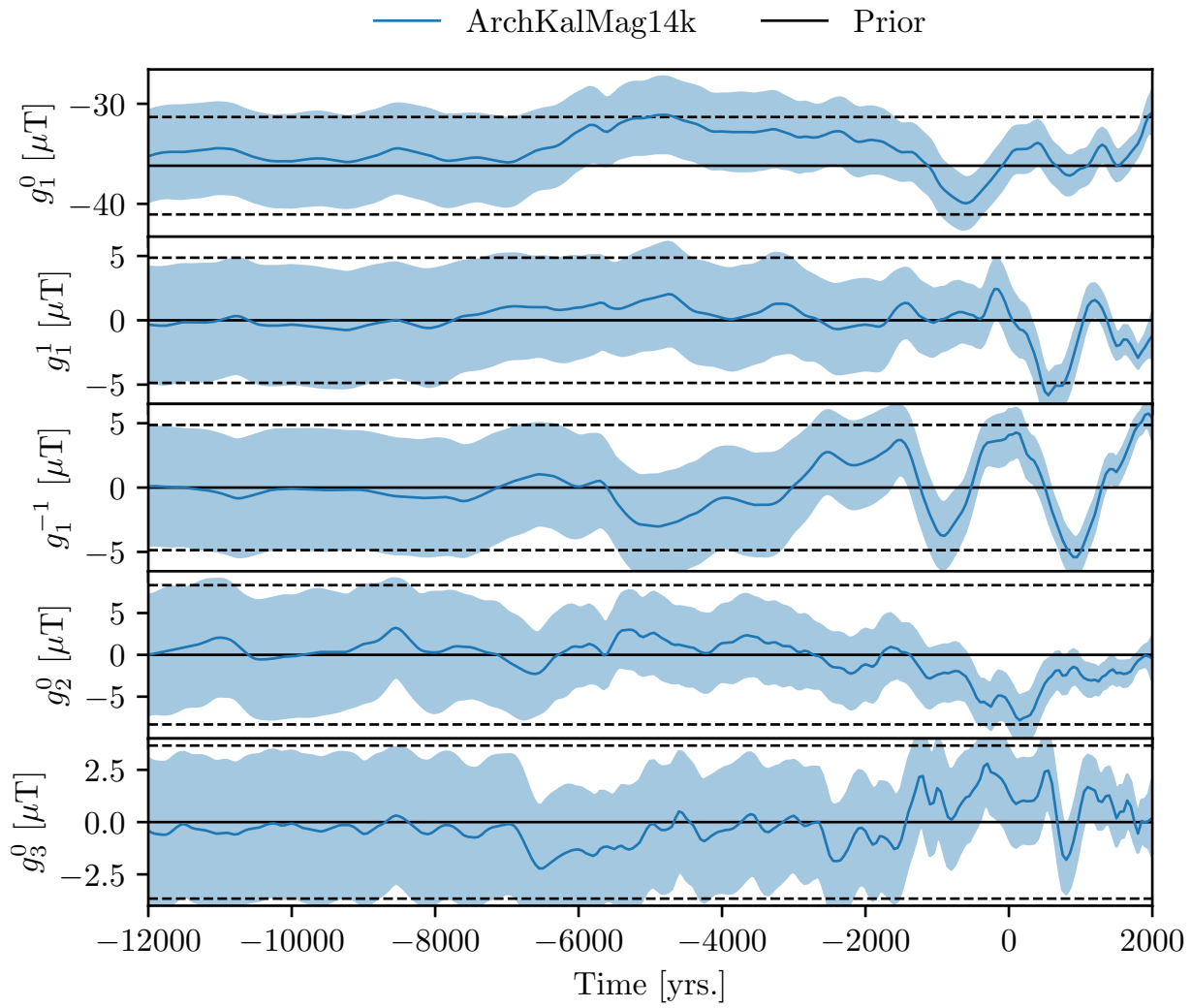


**Figure S2.** ArchKalMag14k model coefficients together with the prior. The shaded area and dashed lines cover 95%.

**Table S1.** Updates to the GEOMAGIA dataset (Brown et al., 2015) used to assemble the database for ArchKalMag14k. GEOMAGIA provides a unique ID for every record, that we use to identify the records from Mexico that we changed, as they have wrong age and dating uncertainty estimates (Mahgoub, pers. comm.). Records with IDs 11237, 2773, 6891 and 13149 have been removed from the dataset as no updated information is available.

UID	Updated age [yrs.]	Updated standard deviation [yrs.]
13153	-7550	422
2768	-8523	800
2769	-7450	270
11967	-10000	338
6893	-10000	338
11966	-5707	184
2770	1250	5
6892	1250	5
13086	8	62
13118	8	62
11992	1545	94